



1     **Dominant synoptic patterns associated with the decay process of**  
2                     **PM<sub>2.5</sub> pollution episodes around Beijing**

3                     Xiaoyan Wang<sup>1,2,3\*</sup>, Renhe Zhang<sup>1,2</sup>, Yanke Tan<sup>1,2</sup>, Wei Yu<sup>1,4</sup>

4     <sup>1</sup>Department of Atmospheric and Oceanic Sciences & Institute of Atmospheric Sciences, Fudan  
5     University, Shanghai, China

6     <sup>2</sup>Big Data Institute for Carbon Emission and Environmental Pollution, Fudan University, Shanghai,  
7     China

8     <sup>3</sup>Shanghai Institute of Pollution Control and Ecological Security, Shanghai, China

9     <sup>4</sup>Shanghai Ecological Forecasting and Remote Sensing Center, Shanghai, China

10

11

12     Correspondence to: Xiaoyan Wang (wangxyfd@fudan.edu.cn)

13

14



## 15 Abstract

16 The variation in the concentrations of ambient PM<sub>2.5</sub> (particles with an aerodynamic diameter less  
17 than 2.5 μm) generally forms a continuous sawtooth cycle with a recurring smooth increase followed  
18 by a sharp decrease. The abrupt decay of pollution episode is mostly meteorological in origin, and  
19 is controlled by the passage of synoptic systems. One affordable and effective measure for the  
20 quickly reducing PM<sub>2.5</sub> concentrations in northern China is to wait for strong wind to arrive.  
21 However, it is still unclear how strong the wind needs to be and exactly what kind of synoptic system  
22 most effectively results in the rapid decay of air pollution episodes. PM<sub>2.5</sub> variations over the 28  
23 pollution channel cities of Beijing are investigated to determine the mechanisms by which synoptic  
24 patterns affect the decay processes of pollution episodes. This work shows more obvious day-to-  
25 day variations in PM<sub>2.5</sub> concentration in winter than in summer, which implies that wintertime  
26 PM<sub>2.5</sub> variations are more sensitive to meteorological factors. There were 365 decay processes from  
27 January 2014 to March 2020, and 97 of them were related to the effective wet deposition. 26%–43%  
28 of PM<sub>2.5</sub> pollutant is removed by the wet deposition in different seasons. Two dominant circulation  
29 patterns are identified in summer, and the same three circulation types (CTs) are identified in the  
30 other three seasons based on the dry-day cases. The circulation patterns beneficial to the decay  
31 processes all exhibit a higher than normal surface wind speed, a negative relative humidity anomaly  
32 and positive divergence in the PM<sub>2.5</sub> horizontal flux. In addition, CT1 in spring, autumn and winter  
33 is controlled by northeasterly wind and features the most significant horizontal net-outflow of air  
34 pollutants and effective upward spread of air pollutants to the free atmosphere, which promotes the  
35 abrupt reduction of local PM<sub>2.5</sub> concentrations. CT2 is the most frequent synoptic pattern leading  
36 to decay processes in autumn and winter, and the domain region is located to the east of an  
37 anticyclone system. CT2 features a strong northwesterly wind of 2.98–3.88 m/s, the lowest relative  
38 humidity and the highest boundary layer height (BLH) among the three CTs, all of which are  
39 favorable for the reduction of PM<sub>2.5</sub> concentrations. In CT3, a prevailing westerly wind anomaly  
40 occurs in the domain, with remarkable zonal divergence in the PM<sub>2.5</sub> flux and strong horizontal  
41 wind shear in the near-surface under the boundary layer. PM<sub>2.5</sub> concentrations show significant  
42 decreases of more than 37%, 41% and 27% after the passage of CT1, CT2 and CT3, respectively. A  
43 dry air mass with a positive BLH anomaly and the effective horizontal outflow of air pollutants are  
44 the main reasons for the abrupt decay phase in summer. PM<sub>2.5</sub> concentrations after the decay  
45 process show a significant decreasing trend from 2014 to 2020, reflecting successful emission  
46 mitigation. Emission reductions have led to a 4.3–5.7 μg/(m<sup>3</sup>.yr) decrease in PM<sub>2.5</sub> concentrations  
47 in the 28 pollution channel cities of Beijing.

48



## 49 1. Introduction

50 PM<sub>2.5</sub> pollution (particles with an aerodynamic diameter less than 2.5 μm) has become a severe  
51 threat and challenge in China, especially in the Beijing-Tianjin-Hebei (BTH) region, and has  
52 attracted significant concern regarding how to improve regional air quality (Che et al., 2019; Wang  
53 et al., 2019a; Xia et al., 2016; Zhang et al., 2018; Mu and Zhang, 2014; Cai et al., 2017; Wang et al.,  
54 2015). To avoid the severe negative impacts of air pollution on public health, the Chinese  
55 government has issued a number of policies to improve the atmospheric environment (Ding et al.,  
56 2019; Chen and Wang, 2015; Zhao et al., 2019; Li et al., 2018b). For example, in September 2013,  
57 the State Council issued the Air Pollution Prevention and Control Action Plan (referred to as Clean  
58 Air Action), which required the BTH region to reduce its PM<sub>2.5</sub> concentrations by 25% within 5  
59 years (China's State Council, 2013). With the deep research on the prevention and control of air  
60 pollution, the regional effects of air pollution from cities in the pollution transmission channel in  
61 the BTH region have been highlighted (China Daily, 2017). Therefore, the Work Plan for Air  
62 Pollution Prevention and Control in Beijing, Tianjin, and Hebei and Surrounding Areas was released  
63 in March 2017 (China's State Council, 2018). Much stricter, more comprehensive, and more  
64 detailed prevention and control measurements were taken in the "2+26" cities, including Beijing,  
65 Tianjin, and 26 other cities in the provinces of Hebei, Shandong, Henan and Shanxi. Due to the  
66 persistent efforts towards emission mitigation, the air quality has shown significant improvement in  
67 these 28 pollution channel cities in recent years (Zhang et al., 2019a; Zhang et al., 2019b; Zheng et  
68 al., 2018; Wang et al., 2019d; Gui et al., 2020).

69 Meteorological conditions are considered as one of the important factors for the variation in ambient  
70 PM<sub>2.5</sub> pollution, especially for the temporal evolution of each air pollution episode (Zhang et al.,  
71 2014; Ma and Zhang, 2020; Wang et al., 2019c). Even under the conditions of a significant decrease  
72 in air pollutant emissions, similar to the COVID-19 lockdown period, PM<sub>2.5</sub> pollution events still  
73 occur frequently in the 28 pollution channel cities due to the unfavorable meteorological  
74 background (Shi and Brasseur, 2020; Le et al., 2020; Huang et al., 2020b; Wang et al., 2020b; Wang  
75 and Zhang, 2020b). Many studies have been conducted and have suggested that multiple  
76 meteorological factors influence the emission of primary pollutants, the formation of secondary  
77 particles and the processes of transport, accumulation and deposition of particles (Zhao et al.,  
78 2020a; Huang et al., 2020c; Chen et al., 2019; Gong and Liao, 2019). High temperatures result in  
79 greater emissions of PM<sub>2.5</sub> precursors and secondary pollutants, and promotes photochemical  
80 reactions, causing an increase in local PM<sub>2.5</sub> concentrations (Zhang, 2017; Zhao et al., 2018b; Chen  
81 et al., 2020). Humidity strongly affects PM<sub>2.5</sub> concentrations in China, especially during severe  
82 pollution episodes (Zhao et al., 2018a; Li et al., 2018a; Huang et al., 2020a). Higher humidity is



83 beneficial for the hygroscopic increase in aerosols and facilitates the formation of secondary  
84 particles (Wang et al., 2019b;Zhao et al., 2017;Cheng et al., 2015;Xin et al., 2016). The cross-  
85 regional transport and horizontal diffusion of pollutants are strongly determined by the wind field.  
86 Southerly winds bring higher concentrations of air pollutants and more moisture, which enhances  
87 the local air pollution in Beijing and the surrounding regions (He et al., 2020;Zhao et al., 2020b). In  
88 addition to individual meteorological variables, synoptic circulation characteristics control the  
89 formation and development of air pollution events (Wang et al., 2020a;Miao et al., 2020;Wang and  
90 Zhang, 2020a; Liu et al., 2019). Monsoonal flows and cold frontal passages are the dominant  
91 meteorological modes controlling the day-to-day variations in PM<sub>2.5</sub> concentrations in the northern  
92 China (Li et al., 2016;Wu et al., 2017;Zhang et al., 1996;Leung et al., 2018). Weak synoptic patterns  
93 with high-pressure or persistent low-pressure systems favor the accumulation of pollutants, while,  
94 strong synoptic patterns with large pressure gradients encourage the diffusion of pollutants (Cai  
95 et al., 2020;Zhang et al., 2017;Zhang et al., 2020;Li et al., 2019). Severe haze events in the BTH region  
96 are always accompanied by stagnant air conditions, stable stratification, weak surface wind, low  
97 boundary layer height (BLH), and high relative humidity (Ma et al., 2020;Bi et al., 2014;Wang et  
98 al., 2020c;Tang et al., 2016;Quan et al., 2020;Pei et al., 2020;Guo et al., 2019).

99 Most of the aforementioned studies focused on the synoptic pattern characteristics favorable for the  
100 initiation and development of air pollution episodes in the BTH region. During the developing phase  
101 of each PM<sub>2.5</sub> pollution episode, the comprehensive effects of secondary aerosol formation,  
102 hygroscopic increase and accumulation of particles lead to an increase in local PM<sub>2.5</sub>  
103 concentrations, which usually takes several days from a clean situation to the outbreak of a heavy  
104 haze (Sun et al., 2014;Wang et al., 2016;Pei et al., 2018). Both atmospheric chemistry and physics  
105 processes play important roles in the developing phase of air pollution events (Gu et al., 2020;Yao  
106 et al., 2018;Wang et al., 2018;Wang et al., 2010;Li et al., 2017;Gao et al., 2017). However, compared  
107 to the developing phase, which typically features a smooth increase in air pollutant concentrations,  
108 the decay phase of each pollution episode shows a sharp decrease in PM<sub>2.5</sub> concentrations, often in  
109 a few hours. The abrupt decrease in PM<sub>2.5</sub> concentrations is purely meteorological in origin and is  
110 controlled by the passage of synoptic systems, especially cold fronts, which terminate a severe air  
111 pollution episode in the BTH region by strong winds (Zhu et al., 2016;Jia et al., 2008;Ji et al.,  
112 2012;Xin et al., 2012). However, it is still unclear how strong the wind needs to be, exactly what  
113 kind of synoptic systems can effectively terminate air pollution episodes in the BTH region, and  
114 what mechanism is responsible for the rapid reduction in PM<sub>2.5</sub> concentrations in a few hours. The  
115 clarification of these issues will contribute to improving local air quality predictions. The variation  
116 in air quality is generally consistent in the 28 pollution channel cities, especially in the decay phase  
117 of pollution episodes, which indicates that the same synoptic system usually affects the whole region.



118 This study will focus on the region covering these 28 pollution channel cities and reveal the synoptic  
119 circulation pattern that dominates the decay process of PM2.5 pollution events.

## 120 2. Data and Method

### 121 2.1 Dataset

122 The daily mean observed PM2.5 concentrations in the 28 pollution channel cities from January 2014  
123 to March 2020 were obtained from the Ministry of Ecology and Environment of the People's  
124 Republic of China (<https://www.aqistudy.cn/historydata/>). Fig. 1 shows the location of the 28  
125 pollution channel cities and their annual mean PM2.5 concentrations from 2014 to 2019. The four-  
126 times-daily dataset of the fifth-generation European Centre for Medium-Range Weather Forecasts  
127 (ECMWF ERA5) atmospheric reanalysis dataset with a resolution of 0.5°  
128 (<https://cds.climate.copernicus.eu/cdsapp#!/dataset/10.24381/cds.bd0915c6?tab=form>) was used to  
129 describe the meteorological characteristics and synoptic circulation classification.

130 The divergence of local PM2.5 flux can be taken as a metric for the PM2.5 budget in the specific  
131 region, with positive divergence indicating net outflow of air pollutants from the domain region,  
132 and vice versa. The daily mean divergence of the PM2.5 flux over the region of 34-40° N and 112-  
133 118° E is calculated according to Eq.(1):

$$134 \quad D = D_z + D_m = \frac{\partial}{\partial x}(UQ) + \frac{\partial}{\partial y}(VQ) = \sum_{i=1}^n \frac{(U_{Ei}Q_{Ei} - U_{Wi}Q_{Wi})}{2\Delta X} + \sum_{j=1}^m \frac{(V_{Nj}Q_{Nj} - V_{Sj}Q_{Sj})}{2\Delta Y} \quad (1)$$

135 where  $D_z$  and  $D_m$  are the zonal and meridional components of the net divergence of PM2.5 flux for  
136 the specific region. The parameters  $n$  and  $m$  indicate the meridional and zonal grid numbers of the  
137 domain. The subscripts  $E$  and  $W$  mark the variables at the longitudes of the eastern and western  
138 boundaries of the domain. Similarly, the subscripts  $S$  and  $N$  represent the values at the latitudes of  
139 the southern and northern boundaries.  $U_{Ei}$  (units in m/s) indicates the 10 m zonal wind in the  $i$ th grid  
140 of the eastern boundary of the domain.  $Q_{Nj}$  (units in  $\mu\text{g}/\text{m}^3$ ) is the spatially interpolated PM2.5  
141 concentration in the  $j$ th grid at the latitude of the northern boundary.  $\Delta X$  and  $\Delta Y$  represent the zonal  
142 and meridional distance of each grid (units in meters). Due to the limited information on the vertical  
143 distribution of PM2.5 and the horizontal winds are closely related with PM2.5 concentration as  
144 revealed by previous studies, the horizontal divergence of PM2.5 flux is used to evaluate the net  
145 inflow and outflow of local air pollutants in this study.

### 146 2.2 Thresholds for the decay process of air pollution episodes

147 Fig. 2 shows the daily PM2.5 concentration variations of the 28 pollution channel cities from



148 January to March 2019. PM<sub>2.5</sub> concentrations exhibit a recurring smooth increase followed by a  
149 sharp decrease, which is known as a sawtooth cycle (Jia et al., 2008). During the developing phase  
150 of each pollution episode, the PM<sub>2.5</sub> concentrations show the same smoothly increasing trend with  
151 slight differences in the rate of increase and magnitude in the 28 pollution channel cities (i.e., an  
152 average increase trend of  $10.37 \pm 42.2 \mu\text{g}/(\text{m}^3 \cdot \text{day})$  during January to March 2019). The  
153 inhomogeneity of the PM<sub>2.5</sub> concentration increase in the 28 cities, indicating by the large standard  
154 deviation of increase trends (approximate four times the magnitude of increase trend), may be due  
155 to the complicated physiochemical processes of haze formation. By contrast, as shown by dotted  
156 lines in Fig. 2, regional synchronous decreases in PM<sub>2.5</sub> concentrations occur in the decay phase of  
157 pollution episodes with an average trend of  $-50.06 \pm 46.83 \mu\text{g}/(\text{m}^3 \cdot \text{day})$ . Most of the  
158 consistent improvements in air quality in the decay phase can be attributed to the effects of the  
159 synoptic system. Therefore, in this study, if more than 40% of the 28 pollution channel cities with  
160 the day-to-day PM<sub>2.5</sub> concentrations decreased by 30% (relative to the value of the previous day)  
161 or more than 60% of the channel cities with PM<sub>2.5</sub> concentrations decreased by 30% in two  
162 successive days, it can be defined as the occurrence of the decay phase of pollution episodes. If two  
163 consecutive days were defined as the decay phase, only the first day was selected be vailed and  
164 retained. In total, 365 days are identified as the decay phase of pollution episodes from January  
165 2015 to March 2020 (see Fig. 4) and are used for the synoptic pattern classification.

### 166 2.3 Method of synoptic circulation classification

167 The T-mode principal component analysis (PCA) method was used to objectively classify the type  
168 of synoptic system dominating the decay phase of pollution episodes, as this method has an  
169 outstanding performance in terms of the reproduction of predefined types and temporal-spatial  
170 stabilities (Huth et al., 2008; Cavazos, 2000; Tie et al., 2015; Valverde et al., 2015; Xu et al., 2016).  
171 The T-mode PCA has been widely used to investigate the general circulation patterns, climate  
172 change and air quality and has been incorporated into the European Cooperation in Science and  
173 Technology (COST) plan 733 toolbox (COST733: <http://cost733.geo.uni-augsburg.de/cost733wiki>)  
174 (Philipp et al., 2014). The daily mean geopotential height (Z), U and V components at 925 hPa  
175 on the 365 decay phase days are used for synoptic pattern classification. To exclude the effects of  
176 seasonal variation on atmospheric circulation and to ensure that different synoptic patterns in the  
177 same season are comparable, the T-mode PCA method is applied to the four seasons respectively.  
178 The target region is 32-44° N and 110-122° E, as shown in Fig. 1. For each season, the three input  
179 data matrixes (U, V and Z) have temporal and spatial dimensions, with spatial grids and time series  
180 represented by rows and columns, respectively. To speed up computations of the T-mode PCA in  
181 the COST733 toolbox, each matrix is first divided into 10 subsets. Then, the principal components



182 (PCs) are determined using the singular value decomposition for each subset, and an oblique  
183 rotation is applied to the PCs to achieve better classification effects. The 10 classifications based on  
184 the subsets are evaluated by the chi-square test and the subset with the highest sum is selected and  
185 assigned to a type.

### 186 **3. Results**

#### 187 **3.1 Identification of the occurrence of the decay process of air pollution episodes**

188 The magnitude of the day-to-day variation in PM<sub>2.5</sub> concentrations is an important metric for  
189 recognizing the occurrence of the decay phase of air pollution. Fig. 3 shows the frequency of the  
190 relative day-to-day PM<sub>2.5</sub> concentration differences in the 28 pollution channel cities during the  
191 period of January 2014 to March 2020. Table 1 summarizes the occurrence frequency of the day-  
192 to-day PM<sub>2.5</sub> differences in the specific segment. It shows that a fatter-tailed probability distribution  
193 exists in winter than in summer; thus, winter features a lower probability of weak PM<sub>2.5</sub> variations  
194 and a higher probability of strong PM<sub>2.5</sub> variations, indicating greater day-to-day variability in  
195 PM<sub>2.5</sub> concentrations. In winter, 8.6% of PM<sub>2.5</sub> concentrations decreased by over 60%, and 14.9%  
196 increased by more than 80%, whereas, in summer, the values were only 2.4% and 6.6%. A total of  
197 38.3% of the cases show day-to-day PM<sub>2.5</sub> variations within the range of -20% to 40% in winter,  
198 but where a total of 55.6% is observed in summer. The PM<sub>2.5</sub> variations in spring and autumn  
199 exhibit almost the same distribution patterns, with a relatively higher frequency of strong PM<sub>2.5</sub>  
200 variations in autumn. Generally, the probability distributions in spring and autumn are between  
201 those of summer and winter. The stronger day-to-day decreases in PM<sub>2.5</sub> concentrations,  
202 particularly the sharp wintertime reductions, may be attributable to the passage of a cold front  
203 synoptic system, and the results suggest that the winter PM<sub>2.5</sub> variations are the most sensitive to  
204 synoptic patterns.

205 According to the occurrence of day-to-day PM<sub>2.5</sub> differences in the 28 pollution channel cities, i.e.,  
206 thresholds for the decay phase of air pollution episodes in Section 2.2, 365 decay processes have  
207 been recognized from January 2014 to March 2020. 97 of the 365 decay phases have effective  
208 precipitation more than of 10 mm/day, in which case the abrupt decrease in ambient PM<sub>2.5</sub>  
209 concentrations are assumed to be related to wet deposition. Only the decay processes on dry days  
210 are involved in the synoptic pattern classification in the following work. Figure 4 shows the annual  
211 cycle of the decay process frequencies in the specific year. In most years, the figure shows a two-  
212 peak annual cycle of the decay phase frequency with a valley in summer, and the valley becomes  
213 deeper after removing the rainy cases. There are 105 (105), 62 (21), 86 (56) and 112 (109) decay



214 process days in spring, summer, autumn and winter for all (dry-day) cases, respectively.  
215 Approximately 70% of the regional sharp reduction in summer can be attributed to the effect of wet  
216 deposition.

### 217 **3.2 Classification of the synoptic circulation dominating the decay processes of air pollution** 218 **episodes**

219 T-mode PCA circulation classification has been applied to the dry-day decay process in individual  
220 seasons. Figs. 5 and 6 show the original and anomalous circulation patterns at 925 hPa under each  
221 circulation type (CT) condition. Two dominant circulation types (CTs) are identified in summer, and  
222 three CTs are identified in the other seasons. The three dominant CTs in spring show almost the  
223 same pattern as those of autumn and winter, and only the occurrence frequency of the CTs differ  
224 among the seasons. The strong prevailing northwesterly wind in the CT2 condition is the commonly  
225 accepted synoptic circulation favorable for the rapid decay of pollution episodes in the BTH region,  
226 and CT2 is also the most frequent CT for the decay phase in autumn and winter. A large-scale high-  
227 pressure system covers the region of central-western Mongolia, northern Xinjiang, Inner Mongolia  
228 and Shaanxi Province in China. Deep low pressure is situated in the northeastern China and northern  
229 Japan. The BTH region is located between the east of the anticyclone and west of the cyclone, and  
230 is dominated by strong northwesterly surface winds with the speeds of 2.98~3.88 m/s in different  
231 seasons. The northwesterly wind corresponds to the significant northerly wind anomaly, which is  
232 beneficial for the transport of cold, clean and dry air masses southward. Although it shows  
233 downward motion due to the upper westerly wind passing the leeward side (see Fig. 7), the other  
234 meteorological variables summarized in Fig. 8 reveal that the highest wind speed, the highest  
235 boundary layer height (BLH) and the lowest relative humidity occur under CT2 conditions, all of  
236 which are favorable for the reduction of PM<sub>2.5</sub> concentrations. Fig. 9 exhibits the distribution of  
237 PM<sub>2.5</sub> flux divergence over the region of 34-40° N and 112-118° E, and its zonal and meridional  
238 components, with positive divergence indicating net horizontal outflow of air pollutants from the  
239 BTH region, and negative divergence indicating the opposite. The PM<sub>2.5</sub> flux divergence is found  
240 to have positive values in all three CTs, indicating that the local ambient PM<sub>2.5</sub> concentrations  
241 decrease with the removal of the polluted air mass or the replacement with clean air. The positive  
242 divergence of the PM<sub>2.5</sub> flux in CT2 is mainly contributed by the meridional outflow, which  
243 highlights the effects of the northerly wind anomaly. Clean, dry and strong northwesterly winds in  
244 the CT2 condition are the major drivers of the decay process of air pollution episodes.

245 In CT1 in spring, autumn and winter, a surface high-pressure system initiates from the Siberian  
246 region and slants forward to central Inner Mongolia and the BTH region, resulting in a position that  
247 is more northeastward than the anticyclonic circulation in CT2. Most areas in China are controlled





248 by a high-pressure system. The BTH region is located within on southeastern edge of the high-  
249 pressure center with an anticyclonic horizontal wind shear in the domain. The average surface wind  
250 speed is of 2.63~3.02 m/s, which is higher than the seasonal mean but not as high as that under CT2  
251 conditions. Although all the surface wind speed, BLH and relative humidity show favorable patterns  
252 for air pollutant diffusion under CT1 conditions, the magnitudes of the above anomalies are not as  
253 high as those under CT2 conditions. Therefore, there must be other mechanisms responsible for the  
254 decay process of pollution episode that are distinct from those of CT2, as is generally believed.  
255 According to the anomaly pattern in Fig. 6, the BTH region is located at the south of the anticyclone,  
256 which is dominated by a remarkable northeasterly wind anomaly. This northeasterly wind anomaly  
257 brings clean and dry air masses to the BTH region, and increases the outward and southward  
258 transport of local air pollutants in the meanwhile, which results in the negative relative humidity  
259 anomaly shown in Fig. 8. The net divergence of air pollutants (i.e., positive divergence of the PM<sub>2.5</sub>  
260 flux in Fig. 9) is the most significant under CT1 conditions, indicating the contribution of horizontal  
261 transport to the rapid decay of pollution episodes. In terms of vertical anomaly circulation, the BTH  
262 region is located under the east of a high-level ridge and west of a high-level trough (figure not  
263 shown here), where there is often upper level convergence and cause the surface high-pressure  
264 anomaly to get higher (see Fig. 6). The upper level convergence leads to the vertical sinking in the  
265 east of the BTH region, which also delivers upper dry and clean air to the surface. In addition, as  
266 shown in Fig. 7, the significant clean vertical sinking airflow in the east of the BTH region combined  
267 with the surface easterly wind anomaly results in air movement westward across the domain and  
268 climbs up along the western mountain region. The upward flow carries the near-surface air  
269 pollutants to the upper level of the boundary layer, where the pollution quickly spreads to the free  
270 atmosphere due to the effective entrainment caused by the strong wind shear at the top of the  
271 boundary layer (see Fig. 7). In general, the remarkable horizontal net-outflow of air pollutants,  
272 negative humidity anomaly and effective outward spread of air pollutants to the free atmosphere  
273 promote the abrupt reduction of local PM<sub>2.5</sub> concentrations.

274 CT3 is the dominant synoptic pattern for the decay process in spring, with the highest frequency of  
275 47%, compared with frequencies of 30% and 17% in autumn and winter. In this kind of circulation  
276 pattern, there is only a closed low-pressure system located over the northeastern China, with large  
277 pressure gradients around the cyclone and weak gradients over most parts of China. The BTH region  
278 borders the cyclone system to the northeast, which leads to a prevailing westerly wind with speeds  
279 of 2.29~3.07 m/s. The low-pressure and westerly wind features are more significant based on the  
280 anomalous circulation at 925 hPa in Fig. 6, especially in winter. In the upper 500 hPa, a deep trough  
281 persists in the northern BTH region, bringing cold air masses from the northwest. Similar to CT1  
282 and CT2, negative relative humidity anomalies and positive surface wind speed anomalies are



283 favorable for the decay of pollution episodes. Given the distribution of the BLH, there is no  
284 significant positive anomaly signal in CT3, unlike in CT1 and CT2. Although a moderate BLH is  
285 observed under CT3 conditions, strong vertical wind shear occurs near the surface, as shown in Fig.  
286 7, which improves the more uniform vertical distribution of air pollutants in the boundary layer.  
287 Moreover, obvious horizontal PM<sub>2.5</sub> divergence also provides a possibility for the decay of air  
288 pollution episodes. To be more precise, the zonal divergence of the PM<sub>2.5</sub> flux that dominates the  
289 net divergence of the whole region, rather than the meridional component as the other two  
290 circulation patterns. The inflow of clean and dry air masses combined with the good performance  
291 of boundary layer mixing are the main reasons for the immediate improvement of air quality when  
292 CT3 occurs.

293 In terms of the synoptic patterns in summer, two CTs are classified excluding the effects of wet  
294 deposition. According to the circulation anomaly in Fig. 6, the synoptic pattern of CT1 in summer  
295 is similar to that of CT3 at 925 hPa in other seasons, which is dominated by a northeastern cyclonic  
296 circulation. Dry northwesterly wind occurs in the BTH region, reducing the local relative humidity.  
297 As shown in Fig. 8, the BLH is higher than the seasonal average, indicating an increase in vertical  
298 diffusion space. The zonal positive divergence of the PM<sub>2.5</sub> flux is offset by the negative value in  
299 the meridional direction. The effect of horizontal transport of air pollutants can be ignored in this  
300 situation. Therefore, the decay process of the air pollution episode in the CT1 condition can be  
301 attributed to the dry air mass and higher than normal BLH.

302 In the anomaly pattern of the CT2 condition in summer, the BTH region is located between the  
303 southern portion of a high-pressure system and the northern portion of a low-pressure system, and  
304 is affected by the prevailing northeasterly surface wind. Clean air masses are transported to the BTH  
305 region along with the northeasterly wind, which can be confirmed by the positive divergence in the  
306 PM<sub>2.5</sub> flux in both zonal and meridional directions. Both the negative relative humidity and positive  
307 BLH anomalies in CT2 are beneficial for the reduction of surface PM<sub>2.5</sub> concentrations, but the  
308 magnitude of the anomaly is not as high as those of the CT1 condition. There is no favorable signal  
309 for the diffusion of surface PM<sub>2.5</sub> in terms of the vertical motion in the two synoptic patterns in  
310 summer. It is the effective horizontal outflow that promotes the decay process of pollution episodes.

### 311 3.3 Synoptic circulation effects on the PM<sub>2.5</sub> pollution

312 Section 3.2 shows different physical mechanisms for the rapid decay of air pollution episodes in the  
313 region covering the 28 pollution channel cities. Fig. 10 exhibits the relative difference in PM<sub>2.5</sub>  
314 concentrations between the day before and after the occurrence of the specific synoptic CTs. The  
315 average PM<sub>2.5</sub> differences in the 28 pollution channel cities are summarized in Table 2.  
316 Unsurprisingly, it shows a remarkable decrease in PM<sub>2.5</sub> concentrations when all the circulation



317 patterns dominate the decay process occurs, but it is worth noting that the magnitudes of the decline  
318 vary according to the synoptic patterns. For the case of spring, autumn and winter, CT2 conditions  
319 demonstrate the most significant effects on the abrupt reduction in PM<sub>2.5</sub> concentrations, with a  
320 more than 40% day-to-day decrease in PM<sub>2.5</sub> concentrations in the 28 pollution channel cities in  
321 all three seasons. CT1 conditions are second in terms of the circulation influence in the decay  
322 process of PM<sub>2.5</sub> pollution episodes. The PM<sub>2.5</sub> concentrations decrease quickly by 37.2%, 40.1%  
323 and 36.9% when CT1 conditions occur in spring, autumn and winter, respectively. The CT3  
324 conditions, which are dominated by westerly winds, show a relatively weak ability on control the  
325 decay process of PM<sub>2.5</sub> pollution episodes. Air quality improves by approximately 26~29%  
326 compared with the previous day due to the occurrence of CT3 conditions. In summer, PM<sub>2.5</sub>  
327 concentrations decrease more significantly with the occurrence of CT1 conditions than with the  
328 occurrence of CT2 conditions, indicating more effective diffusion under northwesterly winds than  
329 under northeasterly airflow. Wet scavenging is an effective method for the rapid decay of air  
330 pollution episodes, especially in wintertime. PM<sub>2.5</sub> concentrations drop sharply after the occurrence  
331 of precipitation, with decreases of more than 35% in spring, autumn and winter. 26.2% of PM<sub>2.5</sub>  
332 pollution is removed by the wet deposition in summer, which is the lowest rate among the four  
333 seasons. The relatively clean background may account for the weak wet deposition effects in  
334 summer.

335 Fig. 2 shows the sawtooth cycle variation in PM<sub>2.5</sub> concentrations with a smooth increase followed  
336 by an abrupt decrease. However, the PM<sub>2.5</sub> concentrations do not always increase gradually before  
337 the decay of the pollution episode. Here, the sawtooth cycle is divided into developing and decay  
338 phases, and the interval stage between two decay phases is defined as the developing phase of a  
339 specific pollution episode. As shown in Fig. 11, when the duration of the developing phase is less  
340 than 3-days, air pollutants accumulate gradually to a maximum until the occurrence of decay process  
341 occurs. However, if the developing phase is longer than 3-days, the highest PM<sub>2.5</sub> concentrations  
342 occur on 1-3 days before the passage of a favorable synoptic system, which indicates that the  
343 developing mature stage of pollution episodes (with high level concentrations) usually persist for  
344 several days.

345 The duration of the developing phase not only changes the shape of the sawtooth cycle but also  
346 affects the maximum PM<sub>2.5</sub> concentrations during the pollution episode, as shown in Fig. 12. Most  
347 of the durations of the developing phase are concentrated in the period of shorter than 5-days in  
348 spring, autumn and winter, with average durations of 5.53, 5.86 and 5.36 days, respectively.  
349 Typically, for the cases in spring and autumn, when the durations are less than 5 days, the maximum  
350 PM<sub>2.5</sub> concentrations during the specific air pollution episode increase with an increase in the  
351 developing phase durations; but the concentrations remain unchanged if the duration longer than 5



352 days. In winter, the maximum PM<sub>2.5</sub> concentrations in a specific sawtooth cycle continue to  
353 increase with increases in the interval between two decay processes. Wintertime air pollution can  
354 be exacerbated by the long-term absence of an effective decay process. The frequency of favorable  
355 circulation patterns is relatively lower in summer, which leads to an effective decay process  
356 occurring every 7.45 days. The maximum PM<sub>2.5</sub> concentrations display an upward tendency with  
357 increases in the developing stage durations, but there are some small fluctuations in the mean value  
358 of the highest PM<sub>2.5</sub> concentration due to the limited samples in summer.

359 Emission and meteorological elements are taken as the two most important factors controlling the  
360 variation in PM<sub>2.5</sub>. Many efforts have been made to mitigate the air pollutant emissions in the 28  
361 pollution channel cities, which have achieved remarkable improvements in air quality in recent  
362 years. However, because obvious interannual difference of the meteorological conditions are  
363 observed, there is uncertainty in the evaluation of emission reductions based on the observed PM<sub>2.5</sub>  
364 concentrations. The quantitative evaluation of the effects of emission reduction measures on the  
365 PM<sub>2.5</sub> concentration variation has been a challenge for policy makers and stakeholders. Here, only  
366 the PM<sub>2.5</sub> concentrations observed on the days of decay processes are compared, which excludes  
367 the different effects of meteorological conditions and evaluates the pure effects of emission  
368 reduction from a certain perspective. Fig. 13 shows a significant decline in seasonal mean PM<sub>2.5</sub>  
369 concentrations from 2014 to 2020 in the 28 pollution channel cities. This figure also shows almost  
370 the same rates of decrease in all four seasons, with relatively smaller decreases of 4.8 and 4.3  
371  $\mu\text{g}/(\text{m}^3\cdot\text{yr})$  in spring and winter and greater decreases of 5.7 and 5.2  $\mu\text{g}/(\text{m}^3\cdot\text{yr})$  in summer and  
372 autumn, respectively. The slight difference in the seasonal decreasing tendency is possibly due to  
373 difference in the main sources of air pollutant emissions.

#### 374 **4. Conclusions and Discussion**

375 The variation in ambient air pollutant concentrations generally represents a continuous sawtooth  
376 cycle with a recurring smooth increase followed by a sharp decrease. The combined effects of  
377 emissions, secondary formation of particles and unfavorable meteorological conditions that trigger  
378 the initiation and development of the specific PM<sub>2.5</sub> pollution episodes over several days. In  
379 contrast, the abrupt decay of pollution episodes is mostly due to the passage of favorable synoptic  
380 patterns, and it usually takes a few hours for conditions to transition from hazy to clean air condition.  
381 The detailed atmospheric circulation features and the mechanisms through which they affect the  
382 decay processes of pollution episodes are discussed in this work. A relatively fatter-tailed probability  
383 distribution of day-to-day PM<sub>2.5</sub> concentration over the 28 pollution channel cities is observed in  
384 winter compared with summer, indicating that winter features a lower probability of weak PM<sub>2.5</sub>



385 variations and a higher probability of strong PM<sub>2.5</sub> variations. The probability distribution of day-  
386 to-day PM<sub>2.5</sub> variations in spring and autumn lies between those of summer and winter. A total of  
387 365 decay processes were recognized from January 2014 to March 2020 based on the regional  
388 variation in the day-to-day PM<sub>2.5</sub> concentration difference. 97 of the 365 decay phases were related  
389 to the effective wet deposition, and most of them occurred in summer. For the dry-day decay  
390 processes, 105, 21, 56 and 109 cases occurred in spring, summer, autumn and winter, respectively.  
391 The intervals between two continuous decay processes are 5.53, 7.45, 5.86 and 5.36 days from  
392 spring to winter, respectively.

393 T-mode PCA circulation classification has been applied to the dry-day decay process of the specific  
394 season. Two dominant circulation patterns are identified in summer; three circulation types for the  
395 other three seasons, in addition, it shows almost the same circulation patterns in the three seasons.  
396 The results show that, in all the circulation patterns, a higher than normal surface wind speed, a  
397 negative relative humidity anomaly and positive divergence in the PM<sub>2.5</sub> horizontal flux benefit the  
398 decay processes. However, there are some distinctive features among the different CTs. In spring,  
399 autumn and winter, the dominant CTs are controlled by northeasterly, northwesterly and westerly  
400 surface wind anomalies, respectively. With the prevailing northeasterly flow in CT1, clean and dry  
401 air masses are transported to the BTH region, resulting in the most significant positive divergence  
402 of air pollutants. Moreover, in the vertical direction, air pollutants carried by ascending motion are  
403 quickly mixed into the free atmosphere with the aid of strong vertical wind shear at the top of the  
404 boundary layer. The combined effects of horizontal and vertical diffusion lead to a reduction in  
405 PM<sub>2.5</sub> concentrations by over 36%. The most frequent pattern for the decay phase in autumn and  
406 winter is CT2, in which the BTH region is located in the eastern portion of an anticyclone system  
407 with strong northwesterly wind. CT2 has the highest surface wind speed, lowest relative humidity  
408 and highest BLH among the three CTs, all of which are favorable for the quick decay of pollution  
409 episodes. The PM<sub>2.5</sub> concentrations in the 28 pollution channel cities decrease by more than 40%  
410 after CT2 occurs. In CT3, the BTH region borders the cyclone system to the northeast, which leads  
411 to a prevailing westerly wind anomaly. In addition to the effective zonal divergence in the PM<sub>2.5</sub>  
412 flux, strong horizontal wind shear in the near-surface improves the more uniform vertical  
413 distribution of air pollutants in the boundary layer. After the passage of CT3, 26~29% of local air  
414 pollutants are typically removed. The two dry-day circulation patterns in summer are similar to the  
415 synoptic patterns of CT1 and CT3 in the other three seasons. A dry air mass with a positive BLH  
416 anomaly and the effective horizontal outflow of air pollutants are the main reasons for the abrupt  
417 decay phases in summer. The average PM<sub>2.5</sub> concentrations on decay process days show a  
418 significant decreasing trend from 2014 to 2020, which indicates the success of emission mitigation  
419 efforts. Emission reductions have led to a 4.3~5.7 μg/(m<sup>3</sup>.yr) decrease in PM<sub>2.5</sub> concentrations in



420 the 28 pollution channel cities.

421

422 **Code/Data availability:** Daily PM<sub>2.5</sub> concentration observations at the 28 channel cities were  
423 obtained from the website of Ministry of Ecology and Environment of the People's Republic of  
424 China (<http://106.37.208.233:20035>). Daily four times ECMWF ERA5 dataset during 2014 to 2020  
425 are downloaded from <https://www.ecmwf.int/en/forecasts/datasets/reanalysis-datasets/era5>.  
426 Atmospheric circulation classification was conducted using European Cooperation in Science &  
427 Technology (COST) plan 733 (cost733class software), which can be downloaded at  
428 <http://cost733.met.no>.

429

430 **Author contributions:** XW and RZ designed research. XW, YT and WY performed the analyses  
431 and wrote the paper. All authors contributed to the final version of the paper.

432

433 **Competing interests:** The authors declare that they have no conflict of interest.

434

435 **Acknowledgements:** We thank the support of Fudan University-Tibet University Joint Laboratory  
436 For Biodiversity and Global Change. This research has been funded by the National Natural Science  
437 Foundation of China (grant nos. 41790470, 41805117 and 41975075).

438

### 439 **Figure captions:**

440

441 Figure 1. Annual mean PM<sub>2.5</sub> concentrations in the 28 pollution channel cities of Beijing from 2014  
442 to 2019 (units: µg/m<sup>3</sup>).

443

444 Figure 2. Time series of daily mean PM<sub>2.5</sub> concentrations in the 28 pollution channel cities from  
445 January to March 2019 (units: µg/m<sup>3</sup>).

446



447 Figure 3. Probability distribution of the relative day-to-day difference of PM<sub>2.5</sub> concentrations. The  
448 relative difference is based on the PM<sub>2.5</sub> concentration on the previous day. The distributions in  
449 spring and autumn are combined in the upper panel, and cases in winter and summer are shown at  
450 the bottom.

451

452 Figure 4. Monthly cumulative occurrence of the decay processes of pollution episodes. The orange  
453 curve indicates the decay process occurrences on dry days. In total, 365 decay processes are  
454 identified from January 2014 to March 2020, and 97 of them are associated with precipitation levels  
455 greater than 10 mm/day.

456

457 Figure 5. Distribution of the geopotential height (shaded, units:  $\text{m}^2/\text{s}^2$ ) and wind fields at 925 hPa  
458 for each circulation type. The number over each subplot indicates the occurrence frequency of the  
459 specific circulation type. The solid blue box is the location of the domain region covering the 28  
460 pollution channel cities.

461

462 Figure 6. Distribution of the geopotential height anomalies (shaded, unit:  $\text{m}^2/\text{s}^2$ ) and wind field  
463 anomalies at 925 hPa for each circulation type.

464

465 Figure 7. Zonal averaged profile of the distribution of vertical wind shear anomalies in the domain  
466 region (shaded, units:  $\text{m}/(\text{s}\cdot 100 \text{ m})$ ) and the vertical and zonal circulation anomalies. The green line  
467 indicates the average location of the top of the boundary layer. Zonal wind shear, circulation and  
468 boundary layer height are the average values between 34–40° N. The two dashed lines are the eastern  
469 and western boundaries of the domain (112 to 118° E). The grey region indicates the average altitude  
470 between 34–40° N.

471

472 Figure 8. Boxplot of surface wind speed, boundary layer height (BLH), sea level pressure (slp) and  
473 relative humidity (RH) for each circulation type. The dashed line indicates the seasonal mean of the  
474 specific variables.

475

476 Figure 9. Boxplot of the divergence of PM<sub>2.5</sub> flux over the region of 34–40° N and 112–118° E. The  
477 daily divergence is calculated based on the Eq.(1). Zonal and meridional components are the first



478 and second terms of the formula.

479

480 Figure 10. Distribution of the daily mean PM<sub>2.5</sub> concentrations before and after the occurrence of  
481 decay processes of pollution episodes in the 28 pollution channel cities. The hollow box indicates  
482 the concentration on the decay phase day, and the solid box is the value on the previous day. The  
483 relative differences in the PM<sub>2.5</sub> concentrations after the occurrence of decay process are  
484 summarized in Table 2. The number at the top of each box indicates the sample size used for the  
485 boxplot. The number in the first line is the sample size of the “before” case; and the second line is  
486 for the “after” case.

487

488 Figure 11. The day of the maximum PM<sub>2.5</sub> concentration during each pollution episode varies with  
489 the duration of the developing phase.

490

491 Figure 12. The density plot of the maximum PM<sub>2.5</sub> concentration according to the duration of the  
492 developing phase of pollution episodes. Daily PM<sub>2.5</sub> concentrations are normalized by their  
493 monthly mean value to exclude the effects of seasonal and interannual variations in air quality. A  
494 warmer color indicates a higher density of scatter. Pentagrams mark the average maximum PM<sub>2.5</sub>  
495 concentration for the specific duration period.

496

497 Figure 13. Variations in the average PM<sub>2.5</sub> concentration on all the decay phase days from 2014 to  
498 2020. The black hollow circles indicate the mean PM<sub>2.5</sub> concentration in each year. The black line  
499 is the fitting line based on the mean value. The number in the subplot is the linear trend of the fitting  
500 line.

501





## 502 References

- 503 Bi, J., Huang, J., Hu, Z., Holben, B., and Guo, Z.: Investigating the aerosol optical and radiative  
504 characteristics of heavy haze episodes in Beijing during January of 2013, *J. Geophys. Res. Atmos.*, 119,  
505 9884-9900, 2014.
- 506 Cai, W., Li, K., Liao, H., Wang, H., and Wu, L.: Weather conditions conducive to Beijing severe haze  
507 more frequent under climate change, *Nat. Clim. Chang.*, 7, 257-262, 2017.
- 508 Cai, W., Xu, X., Cheng, X., Wei, F., Qiu, X., and Zhu, W.: Impact of “blocking” structure in the  
509 troposphere on the wintertime persistent heavy air pollution in northern China, *Sci. Total Environ.*,  
510 140325, 2020.
- 511 Cavazos, T.: Using self-organizing maps to investigate extreme climate events: An application to  
512 wintertime precipitation in the Balkans, *J. Clim.*, 13, 1718-1732, 2000.
- 513 Che, H., Xia, X., Zhao, H., Dubovik, O., Holben, B. N., Goloub, P., Cuevas Agulló, E., Estelles, V., Wang,  
514 Y., and Zhu, J.: Spatial distribution of aerosol microphysical and optical properties and direct radiative  
515 effect from the China Aerosol Remote Sensing Network, *Atmos. Chem. Phys.*, 19, 11843-11864, 2019.
- 516 Chen, H., and Wang, H.: Haze days in North China and the associated atmospheric circulations based on  
517 daily visibility data from 1960 to 2012, *J. Geophys. Res. Atmos.*, 120, 5895-5909, 2015.
- 518 Chen, S., Zhang, X., Lin, J., Huang, J., Zhao, D., Yuan, T., Huang, K., Luo, Y., Jia, Z., and Zang, Z.:  
519 Fugitive road dust PM<sub>2.5</sub> emissions and their potential health impacts, *Environ. Sci. Technol.*, 53, 8455-  
520 8465, 2019.
- 521 Chen, Z., Chen, D., Zhao, C., Kwan, M.-p., Cai, J., Zhuang, Y., Zhao, B., Wang, X., Chen, B., and Yang,  
522 J.: Influence of meteorological conditions on PM<sub>2.5</sub> concentrations across China: A review of  
523 methodology and mechanism, *Environ. Int.*, 139, 105558, 2020.
- 524 Cheng, Y., He, K.-b., Du, Z.-y., Zheng, M., Duan, F.-k., and Ma, Y.-l.: Humidity plays an important role  
525 in the PM<sub>2.5</sub> pollution in Beijing, *Environ. Pollut.*, 197, 68-75, 2015.
- 526 China’s State Council: Notice of the General Office of the State Council on Issuing the Air Pollution  
527 Prevention and Control Action Plan: [http://www.gov.cn/zwggk/2013-09/12/  
528 content\\_2486773.htm](http://www.gov.cn/zwggk/2013-09/12/content_2486773.htm), (last access: 4 August 2020), 2013.
- 529 China’s State Council: The State Council rolls out a three-year ac- tion plan for clean air:  
530 [http://www.gov.cn/zhengce/  
531 content/2018-07/03/content\\_5303158.htm](http://www.gov.cn/zhengce/content/2018-07/03/content_5303158.htm), (last access: 4 August 2020),  
2018.
- 532 China Daily, Air pollution targeted in 28 cities: [http://www.chinadaily.com.cn/china/2017-  
533 08/26/content\\_31131288.htm](http://www.chinadaily.com.cn/china/2017-08/26/content_31131288.htm), (last access: 4 August 2020), 2017.
- 534 Ding, A., Huang, X., Nie, W., Chi, X., Xu, Z., Zheng, L., Xu, Z., Xie, Y., Qi, X., and Shen, Y.: Significant  
535 reduction of PM<sub>2.5</sub> in eastern China due to regional-scale emission control: evidence from SORPES in  
536 2011–2018, *Atmos. Chem. Phys.*, 19, 11791-11801, 2019.
- 537 Gao, M., Carmichael, G. R., Wang, Y., Saide, P. E., Liu, Z., Xin, J., Shan, Y., and Wang, Z.: Chemical



- 538 and Meteorological Feedbacks in the Formation of Intense Haze Events, in: *Air Pollution in Eastern Asia: An Integrated Perspective*, Springer, 437-452, 2017.  
539
- 540 Gong, C., and Liao, H.: A typical weather pattern for ozone pollution events in North China, *Atmos. Chem. Phys.*, 19, 13725-13740, 2019.  
541
- 542 Gu, Y., Huang, R.-J., Li, Y., Duan, J., Chen, Q., Hu, W., Zheng, Y., Lin, C., Ni, H., and Dai, W.: Chemical nature and sources of fine particles in urban Beijing: Seasonality and formation mechanisms, *Environ. Int.*, 140, 105732, 2020.  
543  
544
- 545 Gui, K., Che, H., Zeng, Z., Wang, Y., Zhai, S., Wang, Z., Luo, M., Zhang, L., Liao, T., and Zhao, H.: Construction of a virtual PM<sub>2.5</sub> observation network in China based on high-density surface meteorological observations using the Extreme Gradient Boosting model, *Environ. Int.*, 141, 105801, 2020.  
546  
547  
548
- 549 Guo, J., Li, Y., Cohen, J. B., Li, J., Chen, D., Xu, H., Liu, L., Yin, J., Hu, K., and Zhai, P.: Shift in the temporal trend of boundary layer height in China using long-term (1979–2016) radiosonde data, *Geophys. Res. Lett.*, 46, 6080-6089, 2019.  
550  
551
- 552 He, J., Zhang, L., Yao, Z., Che, H., Gong, S., Wang, M., Zhao, M., and Jing, B.: Source apportionment of particulate matter based on numerical simulation during a severe pollution period in Tangshan, North China, *Environ. Pollut.*, 266, 115133, 2020.  
553  
554
- 555 Huang, R. J., He, Y., Duan, J., Li, Y., Chen, Q., Zheng, Y., Chen, Y., Hu, W., Lin, C., Ni, H., Dai, W., Cao, J., Wu, Y., Zhang, R., Xu, W., Ovadnevaite, J., Ceburnis, D., Hoffmann, T., and O'Dowd, C. D.: Contrasting sources and processes of particulate species in haze days with low and high relative humidity in wintertime Beijing, *Atmos. Chem. Phys.*, 20, 9101-9114, 10.5194/acp-20-9101-2020, 2020a.  
556  
557  
558
- 559 Huang, X., Ding, A., Gao, J., Zheng, B., Zhou, D., Qi, X., Tang, R., Wang, J., Ren, C., and Nie, W.: Enhanced secondary pollution offset reduction of primary emissions during COVID-19 lockdown in China, *Natl. Sci. Rev.*, nwa137, 2020b.  
560  
561
- 562 Huang, X., Ding, A., Wang, Z., Ding, K., Gao, J., Chai, F., and Fu, C.: Amplified transboundary transport of haze by aerosol–boundary layer interaction in China, *Nat. Geosci.*, 1-7, 2020c.  
563
- 564 Huth, R., Beck, C., Philipp, A., Demuzere, M., Ustrnul, Z., Cahynová, M., Kyselý, J., and Tveito, O. E.: Classifications of atmospheric circulation patterns: recent advances and applications, *Ann. N. Y. Acad. Sci.*, 1146, 105-152, 2008.  
565  
566
- 567 Ji, D., Wang, Y., Wang, L., Chen, L., Hu, B., Tang, G., Xin, J., Song, T., Wen, T., and Sun, Y.: Analysis of heavy pollution episodes in selected cities of northern China, *Atmos. Environ.*, 50, 338-348, 2012.  
568
- 569 Jia, Y., Rahn, K. A., He, K., Wen, T., and Wang, Y.: A novel technique for quantifying the regional component of urban aerosol solely from its sawtooth cycles, *J. Geophys. Res. Atmos.*, 113, D21309, 2008.  
570
- 571 Le, T., Wang, Y., Liu, L., Yang, J., Yung, Y. L., Li, G., and Seinfeld, J. H.: Unexpected air pollution with marked emission reductions during the COVID-19 outbreak in China, *Science*, 369, 702-706, 2020.  
572
- 573 Leung, D. M., Mickley, L. J., van Donkelaar, A., Shen, L., and Martin, R. V.: Synoptic meteorological modes of variability for fine particulate matter (PM<sub>2.5</sub>) air quality in major metropolitan regions of China, *Atmospheric Chemistry and Physics*, 18, 6733-6748, 2018.  
574  
575



- 576 Li, H., Zhang, Q., Zhang, Q., Chen, C., Wang, L., Wei, Z., Zhou, S., Parworth, C., Zheng, B., and  
577 Canonaco, F.: Wintertime aerosol chemistry and haze evolution in an extremely polluted city of the North  
578 China Plain: significant contribution from coal and biomass combustion, *Atmos. Chem. Phys.*, 17, 4751–  
579 4768, 2017.
- 580 Li, J., Li, C., and Zhao, C.: Different trends in extreme and median surface aerosol extinction coefficients  
581 over China inferred from quality-controlled visibility data, *Atmos. Chem. Phys.*, 18, 3289–3298, 2018a.
- 582 Li, J., Lv, Q., Jian, B., Zhang, M., Zhao, C., Fu, Q., Kawamoto, K., and Zhang, H.: The impact of  
583 atmospheric stability and wind shear on vertical cloud overlap over the Tibetan Plateau, *Atmos. Chem.*  
584 *Phys.*, 18, 7329–7343, 2018b.
- 585 Li, J., Liao, H., Hu, J., and Li, N.: Severe particulate pollution days in China during 2013–2018 and the  
586 associated typical weather patterns in Beijing–Tianjin–Hebei and the Yangtze River Delta regions,  
587 *Environ. Pollut.*, 248, 74–81, 2019.
- 588 Li, Q., Zhang, R., and Wang, Y.: Interannual variation of the wintertime fog–haze days across central and  
589 eastern China and its relation with East Asian winter monsoon, *Int. J. Climatol.*, 36, 346–354, 2016.
- 590 Liu, C., Zhang, F., Miao, L., Lei, Y., and Yang, Q.: Future haze events in Beijing, China: When climate  
591 warms by 1.5 and 2.0° C, *Int. J. Climatol.*, 40, 3689–3700, 2019.
- 592 Ma, J., and Zhang, R.: Opposite interdecadal variations of wintertime haze occurrence over North China  
593 Plain and Yangtze River Delta regions in 1980–2013, *Sci. Total Environ.*, 139240, 2020.
- 594 Ma, Y., Ye, J., Xin, J., Zhang, W., Vilà-Guerau de Arellano, J., Wang, S., Zhao, D., Dai, L., Ma, Y., and  
595 Wu, X.: The stove, dome, and umbrella effects of atmospheric aerosol on the development of the  
596 planetary boundary layer in hazy regions, *Geophys. Res. Lett.*, 47, e2020GL087373, 2020.
- 597 Miao, Y., Che, H., Zhang, X., and Liu, S.: Integrated impacts of synoptic forcing and aerosol radiative  
598 effect on boundary layer and pollution in the Beijing–Tianjin–Hebei region, China, *Atmos. Chem. Phys.*,  
599 20, 5899–5909, 2020.
- 600 Mu, M., and Zhang, R.: Addressing the issue of fog and haze: A promising perspective from  
601 meteorological science and technology, *Sci. China Earth Sci.*, 57, 1–2, 2014.
- 602 Pei, L., Yan, Z., Sun, Z., Miao, S., and Yao, Y.: Increasing persistent haze in Beijing: potential impacts  
603 of weakening East Asian winter monsoons associated with northwestern Pacific sea surface temperature  
604 trends, *Atmos. Chem. Phys.*, 18, 3173–3183, 2018.
- 605 Pei, L., Yan, Z., Chen, D., and Miao, S.: Climate variability or anthropogenic emissions: which caused  
606 Beijing Haze?, *Environ. Res. Lett.*, 15, 034004, 2020.
- 607 Philipp, A., Beck, C., Esteban, P., Kreienkamp, F., Krennert, T., Lochbihler, K., Lykoudis, S. P., Pianko-  
608 Kluczynska, K., Post, P., and Alvarez10, D. R.: cost733class-1.2 User guide, Augsburg, Germany, 10–21,  
609 2014.
- 610 Quan, J., Dou, Y., Zhao, X., Liu, Q., Sun, Z., Pan, Y., Jia, X., Cheng, Z., Ma, P., and Su, J.: Regional  
611 atmospheric pollutant transport mechanisms over the North China Plain driven by topography and  
612 planetary boundary layer processes, *Atmos. Environ.*, 221, 117098, 2020.



- 613 Shi, X., and Brasseur, G. P.: The Response in Air Quality to the Reduction of Chinese Economic  
614 Activities during the COVID-19 Outbreak, *Geophys. Res. Lett.*, e2020GL088070, 2020.
- 615 Sun, Y., Jiang, Q., Wang, Z., Fu, P., Li, J., Yang, T., and Yin, Y.: Investigation of the sources and evolution  
616 processes of severe haze pollution in Beijing in January 2013, *J. Geophys. Res. Atmos.*, 119, 4380-4398,  
617 2014.
- 618 Tang, G., Zhang, J., Zhu, X., Song, T., Munkel, C., Hu, B., Schäfer, K., Liu, Z., Zhang, J., and Wang, L.:  
619 Mixing layer height and its implications for air pollution over Beijing, China, *Atmos. Chem. Phys.*, 16,  
620 2459, 2016.
- 621 Tie, X., Zhang, Q., He, H., Cao, J., Han, S., Gao, Y., Li, X., and Jia, X. C.: A budget analysis of the  
622 formation of haze in Beijing, *Atmos. Environ.*, 100, 25-36, 2015.
- 623 Valverde, V., Pay, M. T., and Baldasano, J. M.: Circulation-type classification derived on a climatic basis  
624 to study air quality dynamics over the Iberian Peninsula, *Int. J. Climatol.*, 35, 2877-2897, 2015.
- 625 Wang, H., Chen, H., and Liu, J.: Arctic sea ice decline intensified haze pollution in eastern China, *Atmos.*  
626 *Oceanic Sci. Lett.*, 8, 1-9, 2015.
- 627 Wang, J., Liu, Y., and Ding, Y.: On the connection between interannual variations of winter haze  
628 frequency over Beijing and different ENSO flavors, *Sci. Total Environ.*, 140109, 2020a.
- 629 Wang, P., Chen, K., Zhu, S., Wang, P., and Zhang, H.: Severe air pollution events not avoided by reduced  
630 anthropogenic activities during COVID-19 outbreak, *Resour. Conserv. Recycl.*, 158, 104814, 2020b.
- 631 Wang, T., Nie, W., Gao, J., Xue, L., Gao, X., Wang, X., Qiu, J., Poon, C., Meinardi, S., and Blake, D.:  
632 Air quality during the 2008 Beijing Olympics: secondary pollutants and regional impact, *Atmos. Chem.*  
633 *Phys.*, 10, 7603-7615, 2010.
- 634 Wang, X., Wang, K., and Su, L.: Contribution of atmospheric diffusion conditions to the recent  
635 improvement in air quality in China, *Sci. Rep.*, 6, 36404, 2016.
- 636 Wang, X., Dickinson, R. E., Su, L., Zhou, C., and Wang, K.: PM<sub>2.5</sub> pollution in China and how it has  
637 been exacerbated by terrain and meteorological conditions, *Bull. Am. Meteorol. Soc.*, 99, 105-119, 2018.
- 638 Wang, X., Wei, H., Liu, J., Xu, B., Wang, M., Ji, M., and Jin, H.: Quantifying the light absorption and  
639 source attribution of insoluble light-absorbing particles on Tibetan Plateau glaciers between 2013 and  
640 2015, *Cryosphere*, 13, 309-324, 2019a.
- 641 Wang, X., Zhang, R., and Yu, W.: The effects of PM<sub>2.5</sub> concentrations and relative humidity on  
642 atmospheric visibility in Beijing, *J. Geophys. Res. Atmos.*, 124, 2235-2259, 2019b.
- 643 Wang, X., and Zhang, R.: Effects of atmospheric circulations on the interannual variation in PM<sub>2.5</sub>  
644 concentrations over the Beijing-Tianjin-Hebei region in 2013-2018, *Atmos. Chem. Phys.*, 20, 7667-  
645 7682, 2020a.
- 646 Wang, X., and Zhang, R.: How Does Air Pollution Change during COVID-19 Outbreak in China?, *Bull.*  
647 *Am. Meteorol. Soc.*, 1-12, 2020b.
- 648 Wang, Y., Duan, J., Xie, X., He, Q., Cheng, T., Mu, H., Gao, W., and Li, X.: Climatic factors and their  
649 availability in estimating long-term variations of fine particle distributions over East China, *J.*



- 650 Geophys. Res. Atmos., 124, 3319-3334, 2019c.
- 651 Wang, Y., Li, W., Gao, W., Liu, Z., Tian, S., Shen, R., Ji, D., Wang, S., Wang, L., and Tang, G.: Trends  
652 in particulate matter and its chemical compositions in China from 2013–2017, *Sci. China Earth Sci.*, 62,  
653 1857-1871, 2019d.
- 654 Wang, Y., Yu, M., Wang, Y., Tang, G., Song, T., Zhou, P., Liu, Z., Hu, B., Ji, D., and Wang, L.: Rapid  
655 formation of intense haze episodes via aerosol-boundary layer feedback in Beijing, *Atmos. Chem. Phys.*,  
656 20, 45-53, 2020c.
- 657 Wu, P., Ding, Y., and Liu, Y.: Atmospheric circulation and dynamic mechanism for persistent haze events  
658 in the Beijing–Tianjin–Hebei region, *Adv. Atmos. Sci.*, 34, 429-440, 2017.
- 659 Xia, X., Che, H., Zhu, J., Chen, H., Cong, Z., Deng, X., Fan, X., Fu, Y., Goloub, P., and Jiang, H.: Ground-  
660 based remote sensing of aerosol climatology in China: Aerosol optical properties, direct radiative effect  
661 and its parameterization, *Atmos. Environ.*, 124, 243-251, 2016.
- 662 Xin, J., Wang, Y., Wang, L., Tang, G., Sun, Y., Pan, Y., and Ji, D.: Reductions of PM<sub>2.5</sub> in Beijing-  
663 Tianjin-Hebei urban agglomerations during the 2008 Olympic Games, *Adv. Atmos. Sci.*, 29, 1330-1342,  
664 2012.
- 665 Xin, J., Gong, C., Wang, S., and Wang, Y.: Aerosol direct radiative forcing in desert and semi-desert  
666 regions of northwestern China, *Atmos. Res.*, 171, 56-65, 2016.
- 667 Xu, J., Chang, L., Qu, Y., Yan, F., Wang, F., and Fu, Q.: The meteorological modulation on PM<sub>2.5</sub>  
668 interannual oscillation during 2013 to 2015 in Shanghai, China, *Sci. Total Environ.*, 572, 1138-1149,  
669 2016.
- 670 Yao, L., Garmash, O., Bianchi, F., Zheng, J., Yan, C., Kontkanen, J., Junninen, H., Mazon, S. B., Ehn,  
671 M., and Paasonen, P.: Atmospheric new particle formation from sulfuric acid and amines in a Chinese  
672 megacity, *Science*, 361, 278-281, 2018.
- 673 Zhang, F., Wang, Y., Peng, J., Chen, L., Sun, Y., Duan, L., Ge, X., Li, Y., Zhao, J., and Liu, C.: An  
674 unexpected catalyst dominates formation and radiative forcing of regional haze, *Proc. Natl. Acad. Sci.*  
675 USA, 117, 3960-3966, 2020.
- 676 Zhang, K., Ma, Y., Xin, J., Liu, Z., Ma, Y., Gao, D., Wu, J., Zhang, W., Wang, Y., and Shen, P.: The  
677 aerosol optical properties and PM<sub>2.5</sub> components over the world's largest industrial zone in Tangshan,  
678 North China, *Atmos. Res.*, 201, 226-234, 2018.
- 679 Zhang, Q., Zheng, Y., Tong, D., Shao, M., Wang, S., Zhang, Y., Xu, X., Wang, J., He, H., and Liu, W.:  
680 Drivers of improved PM<sub>2.5</sub> air quality in China from 2013 to 2017, *Proc. Natl. Acad. Sci. USA*, 116,  
681 24463-24469, 2019a.
- 682 Zhang, R., Sumi, A., and Kimoto, M.: Impact of El Niño on the east Asian monsoon: A diagnostic study  
683 of the '86-87 and '91-92 events, *J. Meteorol. Soc. Japan*, 74, 49-62, 1996.
- 684 Zhang, R., Li, Q., and Zhang, R.: Meteorological conditions for the persistent severe fog and haze event  
685 over eastern China in January 2013, *Sci. China Earth Sci.*, 57, 26-35, 2014.
- 686 Zhang, R.: Warming boosts air pollution, *Nat. Clim. Change*, 7, 238-239, 2017.



- 687 Zhang, X., Xu, X., Ding, Y., Liu, Y., Zhang, H., Wang, Y., and Zhong, J.: The impact of meteorological  
688 changes from 2013 to 2017 on PM<sub>2.5</sub> mass reduction in key regions in China, *Sci. China Earth Sci.*, 62,  
689 1885-1902, 2019b.
- 690 Zhang, Z., Gong, D., Mao, R., Kim, S.-J., Xu, J., Zhao, X., and Ma, Z.: Cause and predictability for the  
691 severe haze pollution in downtown Beijing in November–December 2015, *Sci. Total Environ.*, 592, 627-  
692 638, 2017.
- 693 Zhao, C., Li, Y., Zhang, F., Sun, Y., and Wang, P.: Growth rates of fine aerosol particles at a site near  
694 Beijing in June 2013, *Adv. Atmos. Sci.*, 35, 209-217, 2018a.
- 695 Zhao, C., Wang, Y., Shi, X., Zhang, D., Wang, C., Jiang, J. H., Zhang, Q., and Fan, H.: Estimating the  
696 contribution of local primary emissions to particulate pollution using high-density station observations,  
697 *J. Geophys. Res. Atmos.*, 124, 1648-1661, 2019.
- 698 Zhao, C., Yang, Y., Fan, H., Huang, J., Fu, Y., Zhang, X., Kang, S., Cong, Z., Letu, H., and Menenti, M.:  
699 Aerosol characteristics and impacts on weather and climate over the Tibetan Plateau, *Natl. Sci. Rev.*, 7,  
700 492-495, 2020a.
- 701 Zhao, D., Schmitt, S. H., Wang, M., Acir, I.-H., Tillmann, R., Tan, Z., Novelli, A., Fuchs, H., Pullinen,  
702 I., and Wegener, R.: Effects of NO<sub>x</sub> and SO<sub>2</sub> on the secondary organic aerosol formation from  
703 photooxidation of alpha-pinene and limonene, *Atmos. Chem. Phys.*, 18, 1611–1628, 2018b.
- 704 Zhao, G., Zhao, C., Kuang, Y., Tao, J., Tan, W., Bian, Y., Li, J., and Li, C.: Impact of aerosol hygroscopic  
705 growth on retrieving aerosol extinction coefficient profiles from elastic-backscatter lidar signals, *Atmos.*  
706 *Chem. Phys.*, 17, 12133-12143, 2017.
- 707 Zhao, H., Che, H., Zhang, L., Gui, K., Ma, Y., Wang, Y., Wang, H., Zheng, Y., and Zhang, X.: How  
708 aerosol transport from the North China plain contributes to air quality in northeast China, *Sci. Total*  
709 *Environ.*, 139555, 2020b.
- 710 Zheng, B., Tong, D., Li, M., Liu, F., Hong, C., Geng, G., Li, H., Li, X., Peng, L., and Qi, J.: Trends in  
711 China's anthropogenic emissions since 2010 as the consequence of clean air actions, *Atmos. Chem. Phys.*,  
712 18, 14095-14111, 2018.
- 713 Zhu, X., Tang, G., Hu, B., Wang, L., Xin, J., Zhang, J., Liu, Z., Münkler, C., and Wang, Y.: Regional  
714 pollution and its formation mechanism over North China Plain: A case study with ceilometer  
715 observations and model simulations, *J. Geophys. Res. Atmos.*, 121, 14,574-514,588, 2016.  
716



717 Table 1. Frequency of the relative day-to-day PM<sub>2.5</sub> difference within the specific range.

Relative Difference (%)	<-80	-80~-60	-60~-40	-40~-20	-20~0	0~40	40~80	80~120	>120
MAM	0.4	4.4	9.0	13.5	17.2	31.6	14.3	5.4	3.8
JJA	0.2	2.2	7.6	15.6	20.7	34.9	12.0	4.3	2.3
SON	1.3	5.2	9.1	12.2	14.8	29.4	15.2	6.7	5.7
DJF	1.9	6.7	9.7	12.5	13.1	25.2	15.3	7.9	7.2

718

719

720 Table 2. The average relative difference of PM<sub>2.5</sub> concentrations before and after the occurrence of  
721 decay processes (i.e.,  $(PM_t - PM_{t-1})/PM_{t-1} * 100$ , where PM<sub>t</sub> is the daily mean PM<sub>2.5</sub> concentration on  
722 the decay phase day).

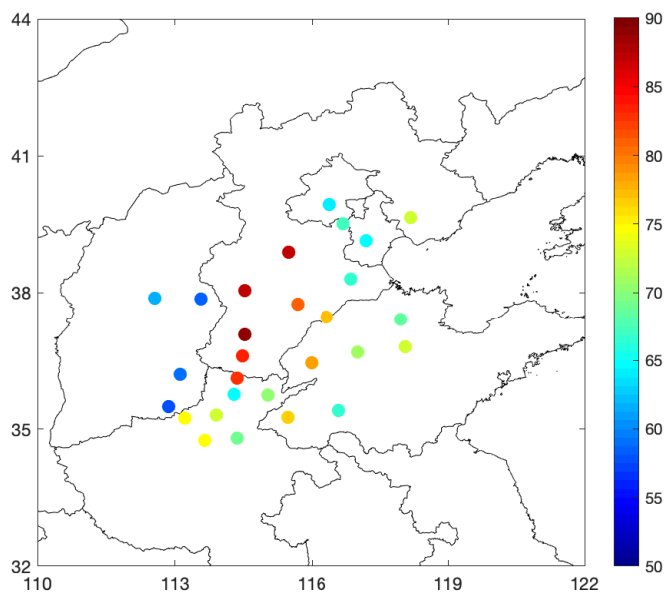
%	CT1	CT2	CT3	Wet deposition
MAM	-37.2	-44.8	-28.2	-40
JJA	-34.5	-20.4	//	-26.2
SON	-40.1	-42.9	-26.9	-35.8
DJF	-36.9	-41	-29.3	-43.9

723

724



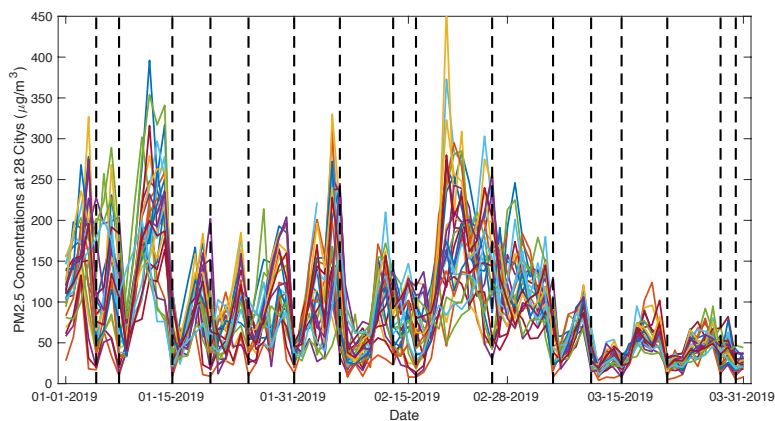
725



726

727 Figure 1. Annual mean PM<sub>2.5</sub> concentrations in the 28 pollution channel cities of Beijing from 2014  
728 to 2019 (units:  $\mu\text{g}/\text{m}^3$ ).

729



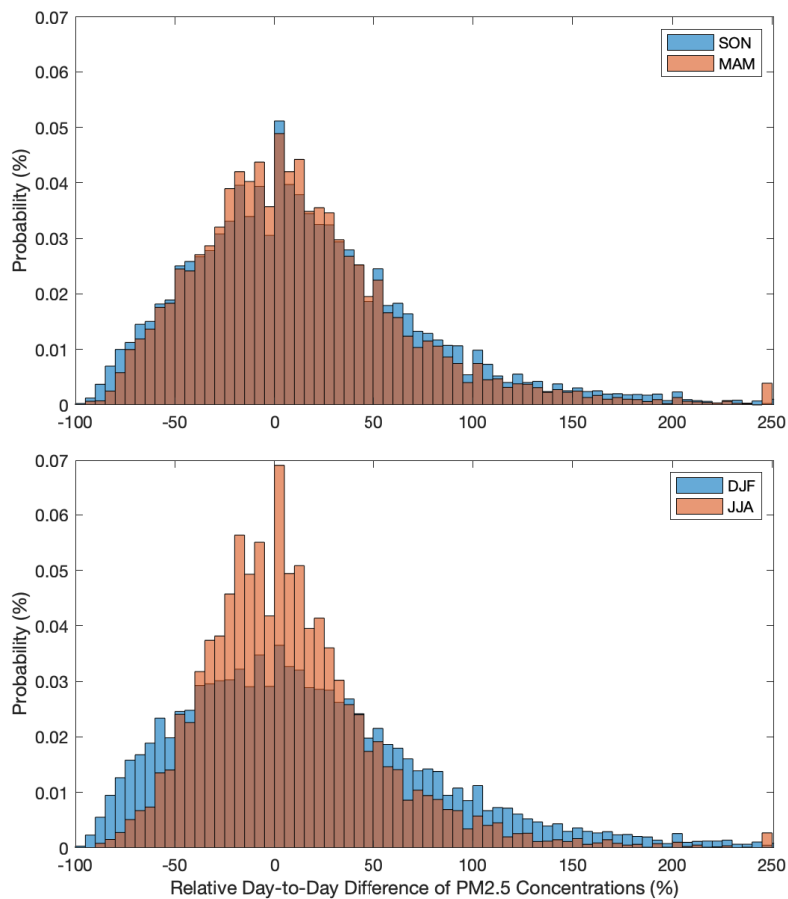
730

731 Figure 2. Time series of daily mean PM<sub>2.5</sub> concentrations in the 28 pollution channel cities from  
732 January to March 2019 (units:  $\mu\text{g}/\text{m}^3$ ).



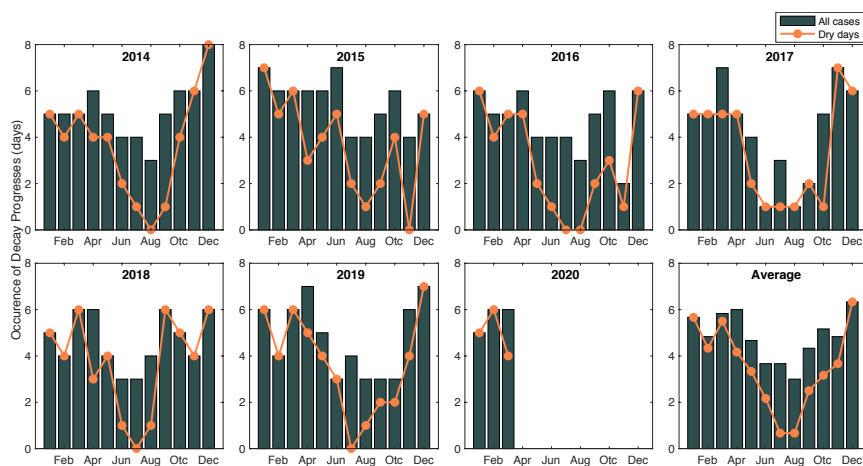


733



734

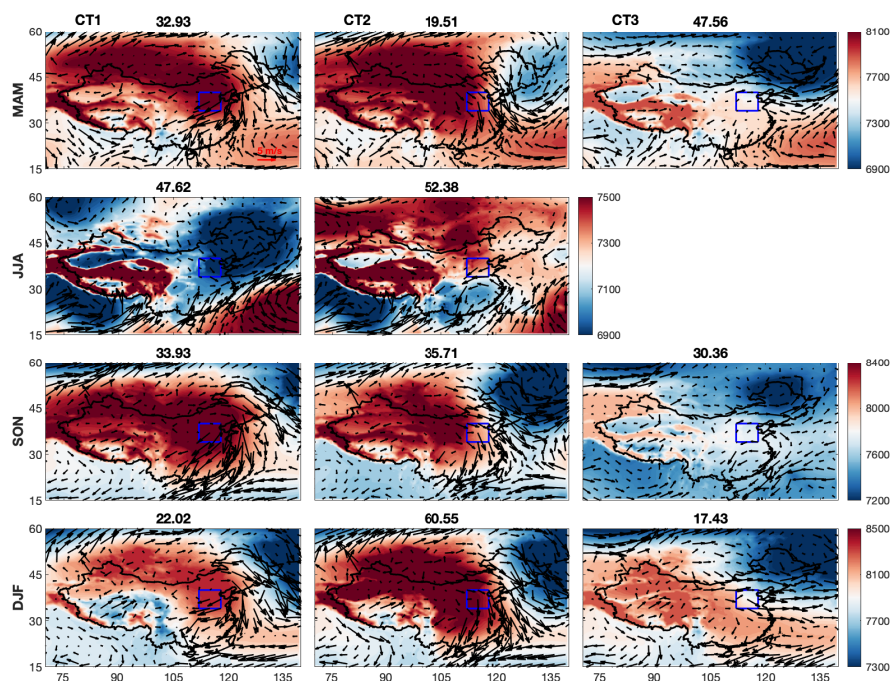
735 Figure 3. Probability distribution of the relative day-to-day difference of PM<sub>2.5</sub> concentrations. The  
736 relative difference is based on the PM<sub>2.5</sub> concentration on the previous day. The distributions in  
737 spring and autumn are combined in the upper panel, and cases in winter and summer are shown at  
738 the bottom.



739

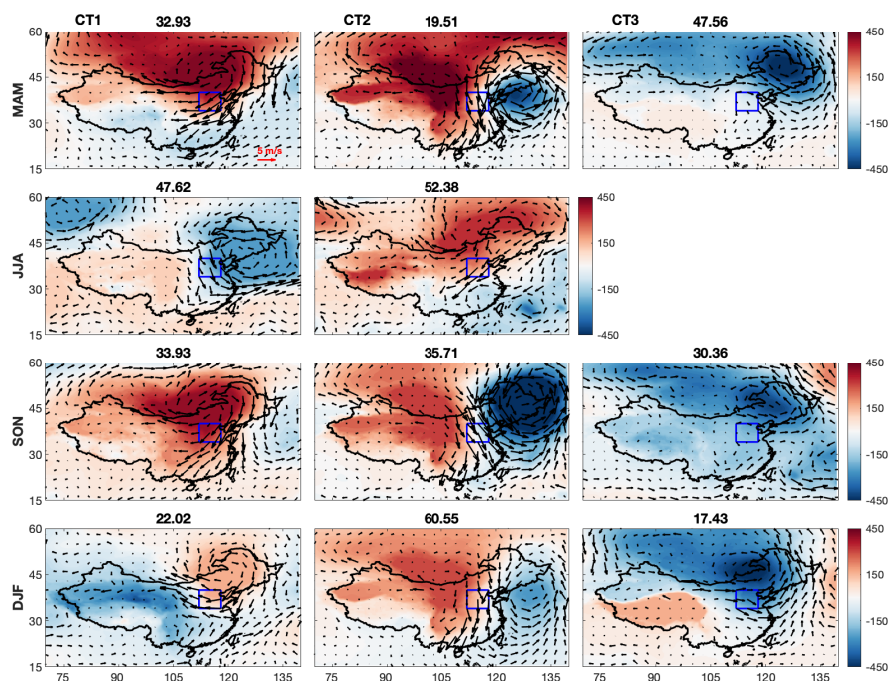
740 Figure 4. Monthly cumulative occurrence of the decay processes of pollution episodes. The orange  
741 curve indicates the decay process occurrences on dry days. In total, 365 decay processes are  
742 identified from January 2014 to March 2020, and 97 of them are associated with precipitation levels  
743 greater than 10 mm/day.

744



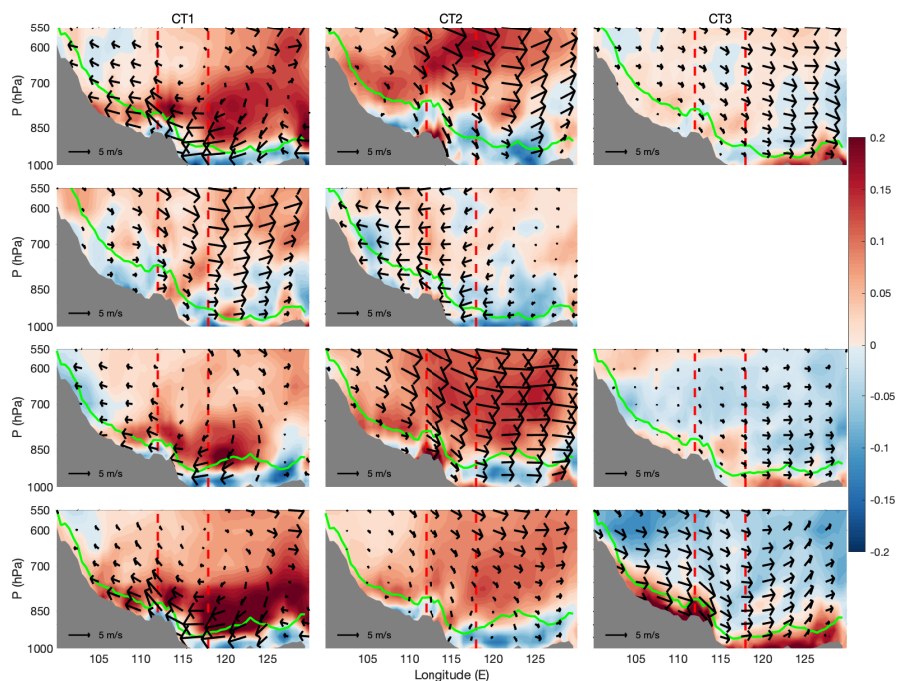
745

746 Figure 5. Distribution of the geopotential height (shaded, units:  $\text{m}^2/\text{s}^2$ ) and wind fields at 925 hPa  
747 for each circulation type. The number over each subplot indicates the occurrence frequency of the  
748 specific circulation type. The solid blue box is the location of the domain region covering the 28  
749 pollution channel cities.



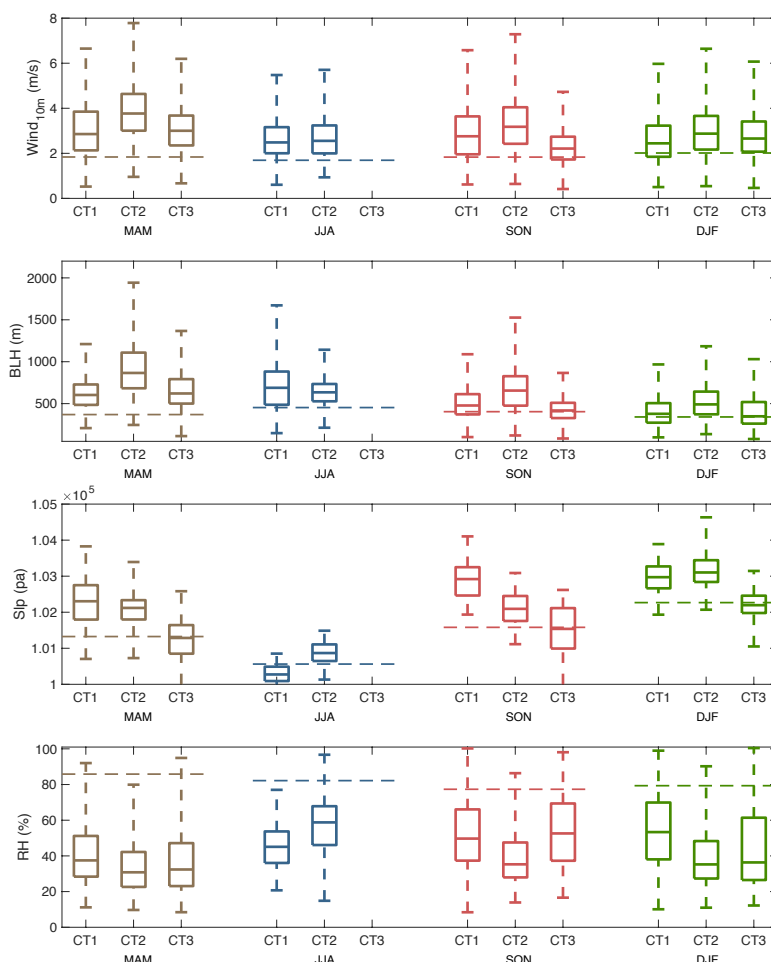
750

751 Figure 6. Distribution of the geopotential height anomalies (shaded, unit:  $\text{m}^2/\text{s}^2$ ) and wind field  
752 anomalies at 925 hPa for each circulation type.



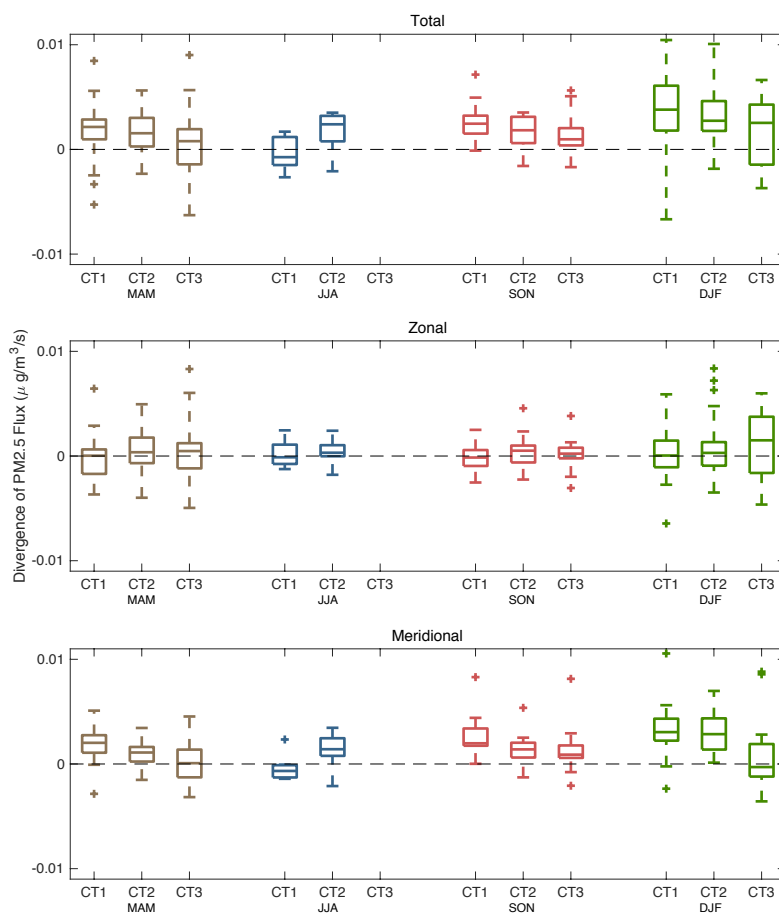
753

754 Figure 7. Zonal averaged profile of the distribution of vertical wind shear anomalies in the domain  
755 region (shaded, units:  $\text{m}/(\text{s} \cdot 100 \text{ m})$ ) and the vertical and zonal circulation anomalies. The green line  
756 indicates the average location of the top of the boundary layer. Zonal wind shear, circulation and  
757 boundary layer height are the average values between  $34\text{--}40^\circ \text{ N}$ . The two dashed lines are the eastern  
758 and western boundaries of the domain ( $112$  to  $118^\circ \text{ E}$ ). The grey region indicates the average altitude  
759 between  $34\text{--}40^\circ \text{ N}$ .



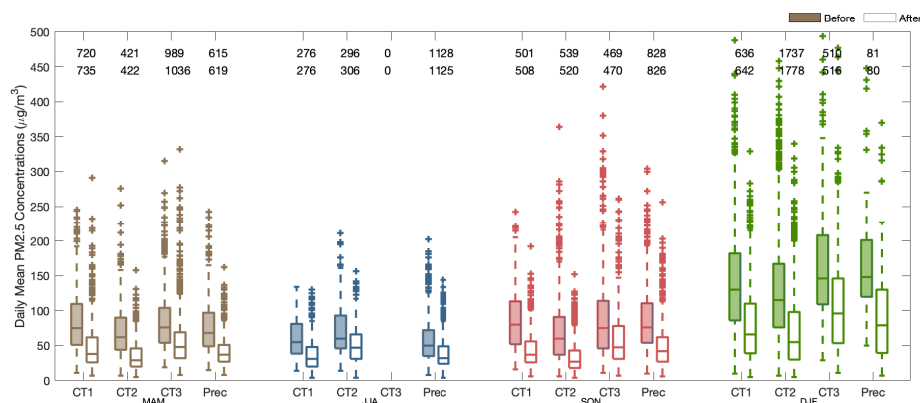
760

761 Figure 8. Boxplot of surface wind speed, boundary layer height (BLH), sea level pressure (slp) and  
762 relative humidity (RH) for each circulation type. The dashed line indicates the seasonal mean of the  
763 specific variables.



764

765 Figure 9. Boxplot of the divergence of PM<sub>2.5</sub> flux over the region of 34–40° N and 112–118° E. The  
766 daily divergence is calculated based on the Eq. (1). Zonal and meridional components are the first  
767 and second terms of the formula.

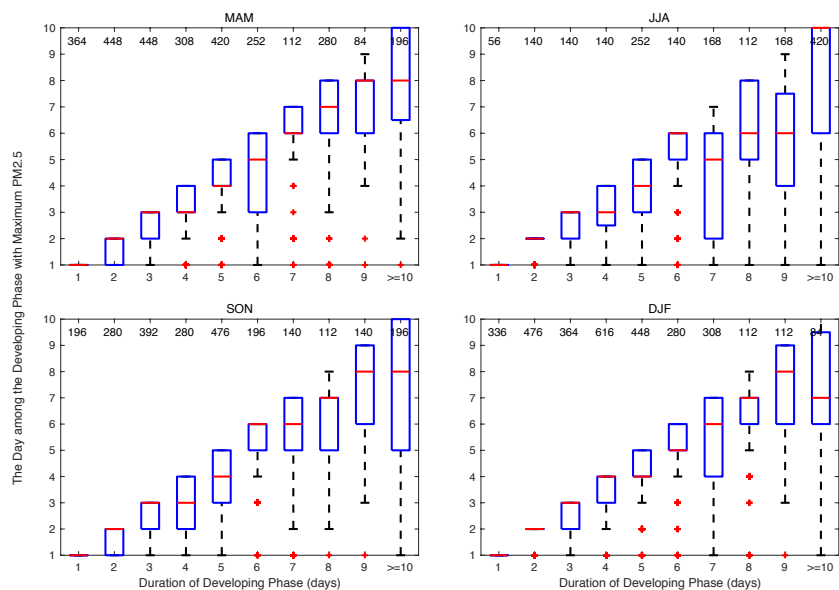


768

769 Figure 10. Distribution of the daily mean PM<sub>2.5</sub> concentrations before and after the occurrence of  
 770 decay processes of pollution episodes in the 28 pollution channel cities. The hollow box indicates  
 771 the concentration on the decay phase day, and the solid box is the value on the previous day. The  
 772 relative differences in the PM<sub>2.5</sub> concentrations after the occurrence of decay process are  
 773 summarized in Table 2. The number at the top of each box indicates the sample size used for the  
 774 boxplot. The number in the first line is the sample size of the “before” case; and the second line is  
 775 for the “after” case.

776

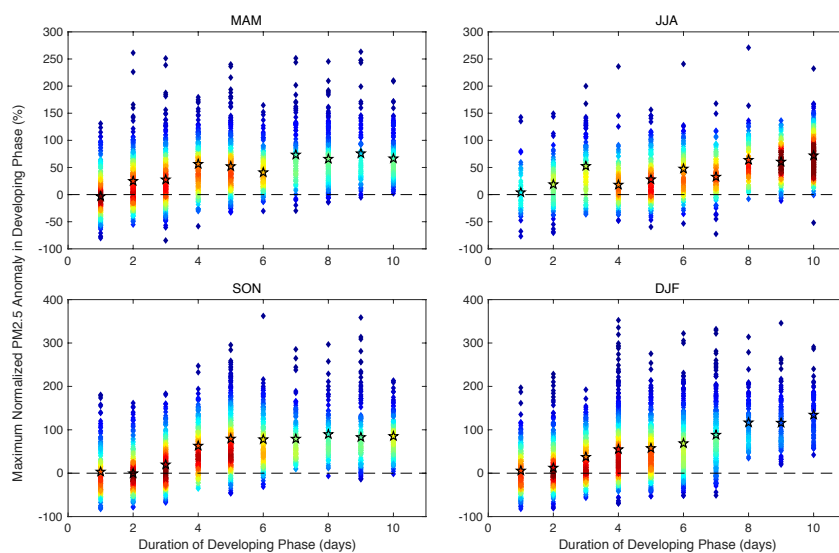




777

778 Figure 11. The day of the maximum PM<sub>2.5</sub> concentration during each pollution episode varies with  
779 the duration of the developing phase.

780



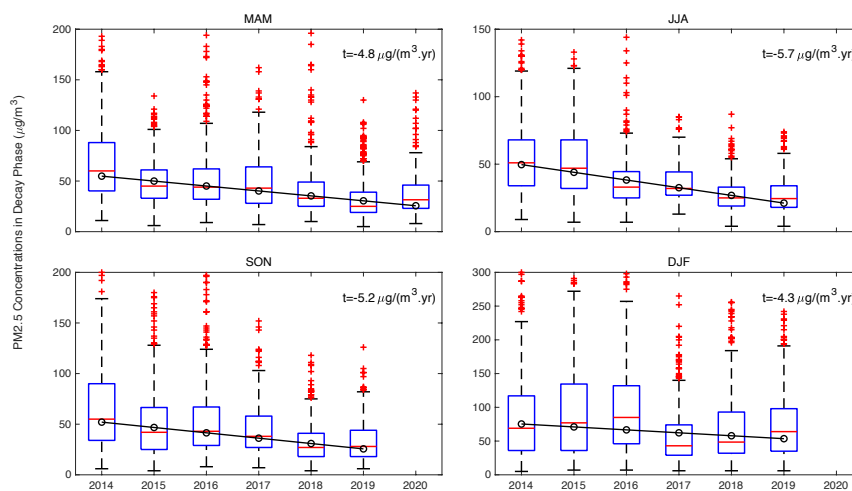
781

782 Figure 12. The density plot of the maximum PM<sub>2.5</sub> concentration according to the duration of the  
783 developing phase of pollution episodes. Daily PM<sub>2.5</sub> concentrations are normalized by their  
784 monthly mean value to exclude the effects of seasonal and interannual variations in air quality. A  
785 warmer color indicates a higher density of scatter. Pentagrams mark the average maximum PM<sub>2.5</sub>  
786 concentration for the specific duration period.

787



788



789

790 Figure 13. Variations in the average PM<sub>2.5</sub> concentration on all the decay phase days from 2014 to  
791 2020. The black hollow circles indicate the mean PM<sub>2.5</sub> concentration in each year. The black line  
792 is the fitting line based on the mean value. The number in the subplot is the linear trend of the fitting  
793 line.

794